Materials Today Physics 28 (2022) 100892

Contents lists available at ScienceDirect

Materials Today Physics

journal homepage: www.journals.elsevier.com/materials-today-physics

Inter-channel conversion between population-/coherence-channel dictates thermal transport in $MAPbI_3$ crystals

Jin Yang [a], Ankit Jain [b], Wee-Liat Ong [a,c,*]

[a] ZJU-UIUC Institute, College of Energy Engineering, Zhejiang University, Jiaxing, Haining, Zhejiang, 314400, China
[b] Mechanical Engineering Department, IIT Bombay, Mumbai, 400076, India
[c] State Key Laboratory of Clean Energy Utilization, Zhejiang University, Hangzhou, Zhejiang, 310027, China

ARTICLE INFO

Keywords:
Hybrid perovskites
Molecular and lattice dynamics
Particle-/wave-nature
Thermoelectrics
Phonons

ABSTRACT

Hybrid halide perovskites, with their favorable carrier recombination time and ultrashort phonon mean-free paths, are leading candidates for various energy conversion applications like photovoltaics and thermoelectrics. The origin of the ultralow thermal conductivity of the prototypical methylammonium lead triiodide ($MAPbI_3$) is of intense research interest as it is critical for improving its energy conversion performance. So far, such an understanding remains elusive in the $MAPbI_3$ above room temperatures (c-$MAPbI_3$) despite numerous efforts due to its unstable phonon modes. Here, we report the discovery of several c-$MAPbI_3$ local minimum energy structures that produce stable phonon dispersions to reveal an amorphous-like coherence-channel thermal transport mechanism in these crystals. Interestingly, an inter-channel conversion between the population- and coherence-channel of the phonons occurs when the c-$MAPbI_3$ changes across these different structures at the same temperature. Such an effect is not yet observed in simple atomic crystals. Our work also shows that existing thermal transport intuitions based on the phonon gas model can be misleading in such hybrid crystals. Further, the dominance of the non-traditional coherence-channel of phonons will affect the interpretation of other phonon-mediated processes in $MAPbI_3$ and other hybrid perovskites.

1. Introduction

Halide perovskites, especially $MAPbI_3$, have been widely studied due to their promising potential in optoelectronic [1–5] and thermoelectric applications [6–8]. Often, $MAPbI_3$-based devices like solar cells operate above room temperature [1,2]. Their thermal stability, lifetime, and efficiency are intimately linked to the thermal transport properties of the $MAPbI_3$. At these temperatures, the $MAPbI_3$ exists as a cubic structure (c-$MAPbI_3$). This structure is deemed inherently unstable due to the rotations of MA cations and the octahedral tilting. Previous harmonic lattice dynamics (HLD) calculations suggest imaginary acoustic phonon modes (aka soft modes) exist near the M and R points of the Brillouin Zone (BZ) [9–13]. Such modes arise from the displacive cubic-to-tetragonal phase transition [12] and the PbI_6 octahedral tilting observed in experiments [13]. Although numerous experimental [14–18] and simulation [9–11,19–21] studies have provided a better understanding of its thermal transport physics, critical questions regarding the phonon characteristics of the c-$MAPbI_3$ remained unanswered due to the existence of these soft modes.

The thermal conductivity of c-$MAPbI_3$ was experimentally measured to be between 0.3 and 0.6 W m^{-1} K^{-1} [14,15]. Results from the classical equilibrium molecular dynamics (EMD) simulations based on the ab-initio derived MYP potential [9,10,21] agree well with these experimental measurements [14,15]. On the other hand, results from the ab initio non-equilibrium molecular dynamics (NEMD) simulations [19] and other EMD simulations based on another potential [20] are about two to three times larger than the experimental values. The differences in the number of atoms, simulated time duration and temperature, and the potentials used could contribute to the discrepancy in the thermal conductivity values. Nevertheless, these MD-based studies typically cannot provide the modal properties of the thermal energy carriers that are essential for understanding and manipulating the thermal transport behavior. To get these modal properties, Zhu et al. [9] and Whalley et al. [11] attempted first-principle anharmonic lattice dynamics [22,23] (ALD) calculations to solve the phonon Boltzmann transport equation [24] (PBTE). In those studies, the imaginary phonon frequencies are either ignored or renormalized using a method that disregards the phonon-phonon interactions. The calculated phonon thermal

* Corresponding author. ZJU-UIUC Institute, College of Energy Engineering, Zhejiang University, Jiaxing, Haining, Zhejiang, 314400, China.
E-mail address: weeong@intl.zju.edu.cn (W.-L. Ong).

https://doi.org/10.1016/j.mtphys.2022.100892
Received 28 August 2022; Received in revised form 9 October 2022; Accepted 14 October 2022
Available online 21 October 2022

conductivity values from the above two approaches are surprisingly similar in magnitude, between 0.04 and 0.06 W m^{-1} K^{-1} but are approximately an order of magnitude lower than the experimental and MYP-based EMD results. This difference was only qualitatively ascribed to the non-phonon nature of the thermal energy carriers in c-$MAPbI_3$ using the Allen-Feldman (AF) framework [9]. Such ad-hoc combinations of possibly inconsistent thermal transport theories with inherently different energy carrier types were also used to explain experimental thermal transport measurements of other complex materials that exhibited crystal-glass duality [25–27].

To investigate the above issues, we employ the lattice dynamics-based phonon Wigner transport equation [28] (PWTE) that inherently captures thermal transport behaviors with the crystal-glass duality. In PWTE, the population-channel (i.e., the particle-like propagation of phonons) and coherence-channel (i.e., the wave-like behaviors of phonons) of the phonon transport contribute simultaneously to the overall thermal conductivity of a material. We like to emphasize that the wave-like coherence-channel transport herein is generally considered different from the coherent phonon transport in superlattices and phononic crystals described in Refs. [27,29–31]. The PWTE can be mathematically reduced to the PBTE for an anharmonic crystal or the AF theory for a harmonic glass, resulting in a unified and consistent treatment of the thermal transport in the different classes of materials using a single type of carrier [32–34]. A stable phonon dispersion is crucial for any lattice dynamics-based method to produce a reliable thermal conductivity study. Such a dispersion has been elusive for c-$MAPbI_3$ due to its unstable structure. To this end, we successfully obtained not one but three stable c-$MAPbI_3$ structures that, for the first time, produced all positive phonon frequencies under an HLD calculation. After comparing these structures with published structural results from experiments, we elucidated the $MAPbI_3$ experimental thermal conductivity trend using the PWTE to discover a coherence-channel thermal transport behavior accounts for more than 70% of its thermal conductivity. A subsequent comparison of the thermal transport characteristics between our optimized structures revealed a mutual compensation between the population- and coherence-channel. This compensation suggests a possible inter-channel conversion between the contributions from the population- and coherence-channel of the phonons in a transport process.

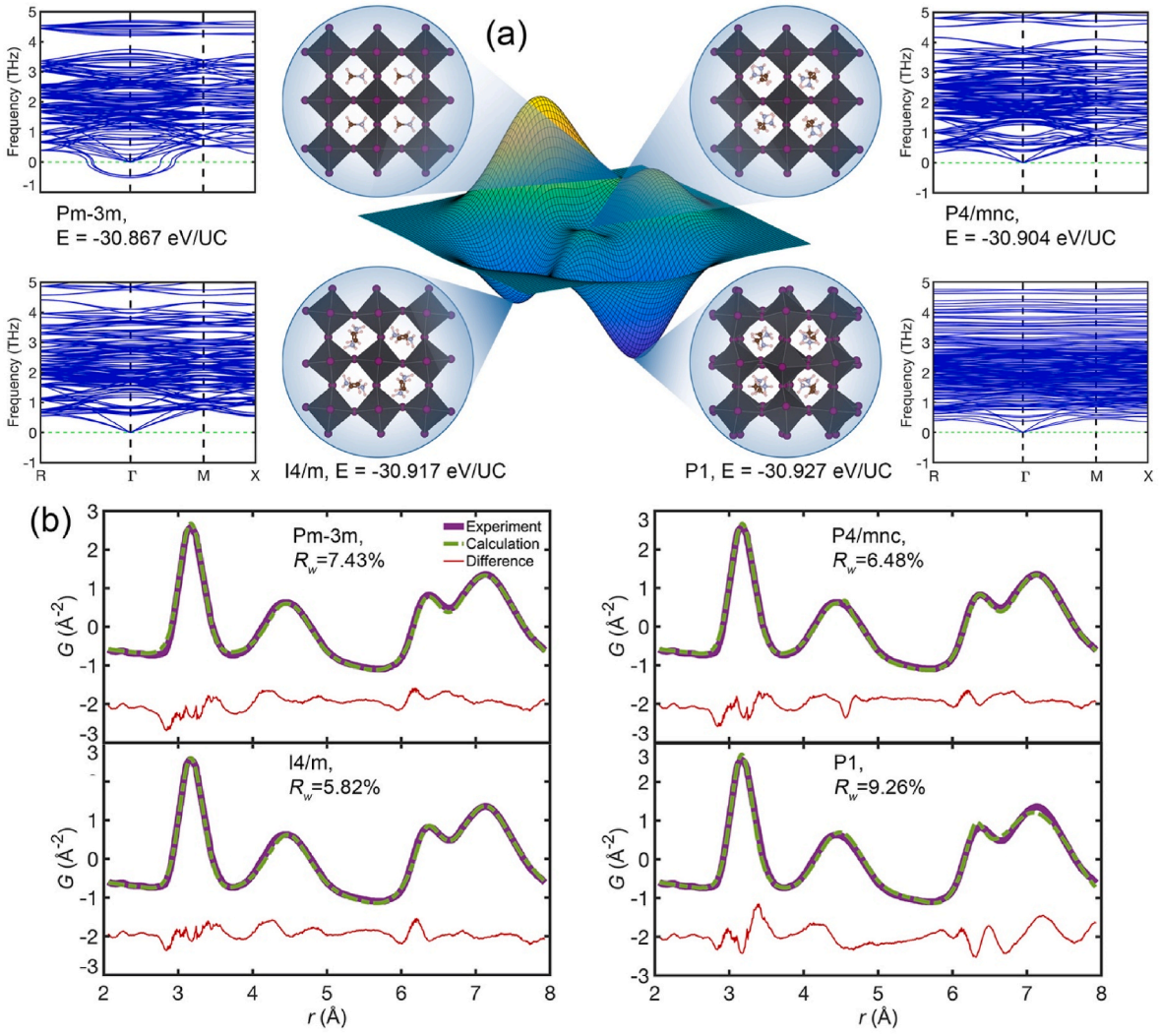

Fig. 1. Four different structures of the c-$MAPbI_3$, the common c-$MAPbI_3$ structure with the *Pm-3m* space group, and three optimized structures with the *P4/mnc*, *I4/m*, and *P*1 space group. (a) Their associated phonon dispersions and potential energies per unit cell (UC) of c-$MAPbI_3$. All structures were visualized using VESTA [41]. The surrounding PES is for illustration purpose only. (b) Comparisons of their PDFs (dotted green) with the experiment PDF [13] (solid purple). The differences (red) between the experiment and calculated PDFs are magnified three times and centered at the level of −2 on the y-axis for clarity.

2. Results

2.1. Optimized c-$MAPbI_3$ structures for harmonic lattice dynamic (HLD) calculations

As mentioned earlier, the HLD calculation performed on the commonly-used 1 × 1 × 1 unit cell of c-$MAPbI_3$ [9–11], which has a *Pm*-3*m* space group, produces imaginary phonons at the BZ boundaries (Fig. S1). These imaginary phonons distort the structure and break the crystal periodicity. This periodicity, however, can be preserved using a larger unit cell in a calculation [35]. The HLD calculations were repeated using a larger 2 × 2 × 2 unit cell that contains 96 atoms (Fig. 1a). Its resulting phonon dispersion depicts the expected "folding" of the phonon branches [35]. The acoustic phonon branches near the 1 × 1 × 1 BZ boundaries were folded into the 2 × 2 × 2 BZ center but remained imaginary. To eliminate these imaginary frequencies, we developed an efficient structure optimization procedure that is possibly simpler than existing works [36,37] (see the Methods) to obtain three distinct 2 × 2 × 2 c-$MAPbI_3$ structures that produce all positive frequencies in their HLD phonon dispersions (Fig. 1a). These structures are strictly cubic with their lattice constants $x = y = z = 12.59$ Å and are of the space group *P4/mnc*, *I4/m*, and *P*1. Details of these optimized structures are available online in the supporting information. As the common *Pm*-3*m* structure has imaginary phonon frequencies at the Γ point, it is probably located on a saddle point in the potential energy surface (PES) [38]. On the other hand, our optimized structures sit at the local energy minima to produce real phonon dispersions. The largest potential energy difference between our optimized structures is 0.023 eV/UC, while the thermal fluctuation at 350 K is bigger at 0.030 eV. This difference suggests that these structures are energetically accessible and interconvertible at 350 K. Although an ensemble-averaged structure is typically used in an HLD calculation [39], such a structure can be challenging to obtain in hybrid crystals like $MAPbI_3$. The positions of the different atoms of a weakly-bounded and rotating MA cation in an ensemble-averaged structure will collapse approximately onto one location, rendering wrong force calculations. In this study, we obtained three different 2 × 2 × 2 structures that can capture different instances of the dynamic disorder induced by the rotations of the MA cations in the c-$MAPbI_3$. These structures approximate the possible snapshots of the $MAPbI_3$ dynamic structure. By discovering more of such structures, we can use them to understand the dynamic disorder in this material.

Next, we compared our structures with existing experimental measurements. As the $MAPbI_3$ crystal is inherently disordered [9], standard Bragg diffraction results from the conventional X-ray crystallographic technique are inadequate to resolve the local structural order. This inadequacy is similar to that seen in the disordered superatomic crystals [27]. However, analyzing the X-ray data using the pair distribution function (PDF) technique can give quantitative insights into the short to intermediate-range structural order regardless of the degree of disorder [40]. The PDF is thus well suited to study the local order, like the octahedral tilting in $MAPbI_3$ as previously performed [13]. Thus, we first compared the PDF of our structures with that from the experiments [13] (Fig. 1b). The fitting difference (R_w) used in Fig. 1b is a simple indicator to show that our structures are reasonable and resemble those in the experiments. However, with the possible noise and the limited resolution in an experimental PDF, using R_w alone is insufficient to judge which of our structures is the most experimentally probable. As seen in Fig. 1b, our 2 × 2 × 2 structures are physically realistic and can produce the real phonon dispersions necessary for detailed phonon-level studies. We would like to stress that these may not be the only structures that can give real phonon dispersions as there can be more local minima in the PES. Also, it is uncommon to use a large number of atoms (i.e., 96 atoms in this study) for lattice dynamics-based calculations due to its high computational cost. This cost problem is further exacerbated in the *P*1 space group structure as it has zero symmetry and cannot be reasonably studied using ALD. For this reason, the following thermal transport study only uses the *P4/mnc* and *I4/m* structures.

2.2. The population- and coherence-channel of phonons in c-$MAPbI_3$ of the *I4/m* space group

The thermal conductivity (κ_{NEMD}) of the c-$MAPbI_3$ was investigated using the NEMD method. By increasing the system length until a size-invariant thermal conductivity is obtained (Fig. S2), our κ_{NEMD} results agree with prior MYP-based EMD and experimental results (Fig. 2). Although the c-$MAPbI_3$ has a Debye temperature of 120 K, which was fitted from experimentally temperature-dependent thermal conductivity [16], its thermal conductivity trend above 327 K is almost invariant and weaker than the expected T^{-1} crystalline behavior from the three phonon scattering processes [42]. Such weak temperature trends were also observed in several novel crystals with complex structures [25–28,32,43,44], pointing to the possibility of an additional non-phonon thermal transport channel.

We investigated the above postulation using the PWTE formalism [28] under the classical and quantum statists (see Methods). Results from the *I4/m* structure are discussed here and compared with those from the *P4/mnc* structure in later sections. In Fig. 2, the κ_{NEMD} values at the different temperatures are almost identical to the PWTE-based $\kappa_{T,Classical}$ values as they are both classical in nature. Regardless of the type of statistics used, the thermal conductivity contributed by the population-channel (i.e., $\kappa_{P,Quantum}$ and $\kappa_{P,Classical}$) is higher than the published DFT-based results [9,11] that used harmonic phonon dispersions with imaginary modes. However, these population-channel contributions account for less than 30% of the total thermal conductivity (i.e., $\kappa_{T,Quantum}$ and $\kappa_{T,Classical}$). The thermal conductivity contribution from the coherence-channel (κ_C) contributes to the rest of κ_T, suggesting a dominant amorphous-like thermal transport nature in the c-$MAPbI_3$ [28].

Four additional insights can be obtained from Fig. 2. First, the $\kappa_{T,Classical}$ at temperatures higher than 327 K are unexpectedly two times larger than the $\kappa_{T,Quantum}$ in the c-$MAPbI_3$, which has a Debye temperature of 120 K [16]. Results under classical statistics usually converge to those under quantum statistics when the temperatures used in the calculations are much higher than a material's Debye temperature [45]. Hence, using the Debye temperature to gauge the suitability of classical statistics may be inaccurate in materials with many high-frequency optical modes that contribute significantly to the overall thermal

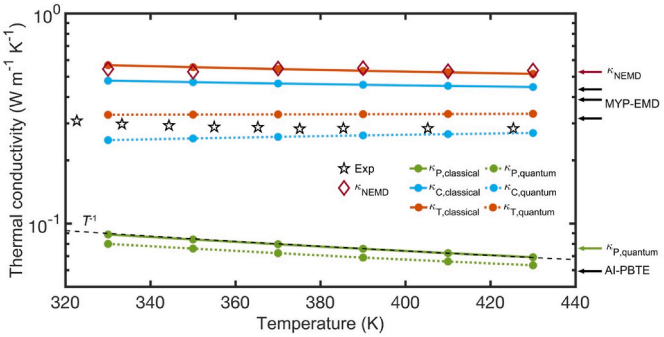

Fig. 2. The thermal conductivity of c-$MAPbI_3$ versus temperature. Exp represents experimental measurements from Ref. [14]. κ_{NEMD} results are from our NEMD simulations, with the associated uncertainty of each point smaller than a marker. κ_T, κ_P, and κ_C are the total thermal conductivity, the population-channel contribution, and the coherence-channel contribution calculated using the PWTE. Both quantum and classical statistics were used, with their results labeled accordingly. κ_P reflects the T^{-1} scaling from the three-phonon scattering. The black arrows on the right y-axis indicate the thermal conductivity values at a temperature of 350 K from other theoretical studies. MYP-EMD are classical MYP-based EMD simulations [9,10,21]. The AI-PBTE are first-principle PBTE results under quantum statistics [9,11].

conductivity through the coherence-channel. Second, similarities between our κ_{NEMD} values from the MD simulations and the $\kappa_{T,Classical}$ values from the PWTE calculations support the suggestions that the rotations of the MA cations have minimal effect on the thermal transport in the c-$MAPbI_3$ [17,46]. MD simulations intrinsically include the rotations of MA cations, whereas PWTE only deals with static structures with fixed orientations of the MA cations. Third, we found that the linear extrapolation technique [47,48] used for extracting a converged thermal conductivity from MD simulations does not work in the c-$MAPbI_3$ (inset of Fig. S2). This extrapolation technique also fail in some amorphous materials [49,50]. One possible reason is that this technique originates from the PGM [47,48] and thus can be incompatible when the coherence-channel of the phonons dominates thermal transport. However, further studies are needed to clarify the reasons behind this failure and whether this linear extrapolation technique is valid for other complex crystalline systems with sizeable coherence-channel contributions. Fourth, as κ_C has amorphous-like thermal transport characteristics, it should increase with increasing temperatures [28]. Our results show that $\kappa_{C,Quantum}$ increases as expected, but $\kappa_{C,Classical}$ decreases instead. This apparent paradox comes from the activation of the higher frequency phonon modes under classical statistics (Fig. S3) that increases phonon scattering. For clarity, quantum statistics is employed to analyze the phonon properties for the rest of this work.

We calculated the phonon characteristics of the c-$MAPbI_3$ at a temperature of 350 K and plotted the results in Fig. 3. Each circle refers to a phonon mode, while the area represents the thermal conductivity contribution. As illustrated in Fig. 3a, almost all of the κ_P comes from the acoustic phonon modes around the BZ center (i.e., green circles). On the other hand, the optical phonons contribute heavily to κ_C (i.e., blue circles). There are also phonon modes that contribute to both channels (i.e., red circles). The thermal conductivity accumulation curves in Fig. 3b indicate that κ_P is higher than κ_C only for phonon frequencies below 0.85 THz. These phonons originate mainly from the vibrations of the inorganic atoms and are acoustic in nature, with their density of states following a Debye-like frequency scaling [51] (Fig. 3c). At higher phonon frequencies, however, κ_C dominates while κ_P plateaus. This result signifies a highly structurally disordered and/or anharmonic crystal structure [28]. As κ_C increases in tandem with the vibrational density of states of the organic and the inorganic entities in c-$MAPbI_3$ (Fig. 3b and c), the whole structure, not just the organic cations, is structurally disordered and/or anharmonic and contributes to κ_C.

2.3. The thermal transport characteristics of the P4/mnc and I4/m structures at a temperature of 350 K

We compared the thermal transport properties of our *P4/mnc* and *I4/m* c-$MAPbI_3$ structures at a temperature of 350 K. The phonon group velocities and lifetimes are plotted for frequencies up to 6.5 THz in Fig. 4a and b. In Fig. 4a, the phonon group velocities of the *P4/mnc* are slower than those of the *I4/m* structure. The average group velocity of the phonons of the *P4/mnc* is about 76.8% of the *I4/m* (Fig. 4c). This reduction comes from the softening of the phonon branches of the *P4/mnc* (Figs. 1a and 4a). As most of the acoustic phonons are from the vibrations of the inorganic PbI_6 octahedra (Fig. 3), these phonons will be directly affected by the octahedral tilting. Such tilting is almost negligible in the less stable *P4/mnc* as compared to that in the *I4/m*. This result suggests that in structures with the same lattice constant, the tilting can stabilize and stiffen the acoustic phonons, similar to that in a $MAPbI_3$ cubic-to-tetragonal transition [12]. Also observed from our phonon dispersions is an accompanied stiffening of some low-frequency optical phonons in the *I4/m*. This octahedral tilting and the reorientation of the MA cations are intimately linked with changes in the (N–H_3)–I hydrogen bonds [52,53]. We found that the average H–I hydrogen bond length is longer in the almost non-tilted *P4/mnc* (Fig. S4), suggesting that these MA cations can move more freely due to their weaker interactions with the inorganic cages. Thus, the anharmonicity is stronger in the *P4/mnc*, as manifested in the shorter phonon lifetimes in Fig. 4b. The average lifetime of the *P4/mnc* is around 30.5% of the *I4/m* (Fig. 4c). With the shorter lifetimes and smaller group velocities, the *P4/mnc* structure gives a κ_P that is six times smaller than the *I4/m* structure (i.e., 0.014 W m^{-1} K^{-1} versus 0.076 W m^{-1} K^{-1} in Fig. 4d). However, the calculated κ_T of both structures are similar at 0.353 W m^{-1} K^{-1} (*P4/mnc*) versus 0.330 W m^{-1} K^{-1} (*I4/m*). The similarity in κ_T is expected as these two structures belong to an identical phase of the same material at the same temperature. This result shows that κ_P and κ_C can mutually compensate to produce the same κ_T, hinting at an inter-channel conversion when the c-$MAPbI_3$ crystal vibrates at a temperature through the different local PES minima. In other words, as this hybrid crystal vibrates at 350 K, the contributions from the population- and coherence-channel of the phonons can actively change, but they sum up to a similar overall thermal conductivity value. This peculiar effect is not seen in studies for simple atomic crystals and remains to be further investigated. As molecular dynamics is assumed to be ergodic and our κ_T and κ_{NEMD} agree closely, these thermal conductivity results also support the validity of our optimized structures. Additionally, the smaller phonon group velocities and lifetimes of the

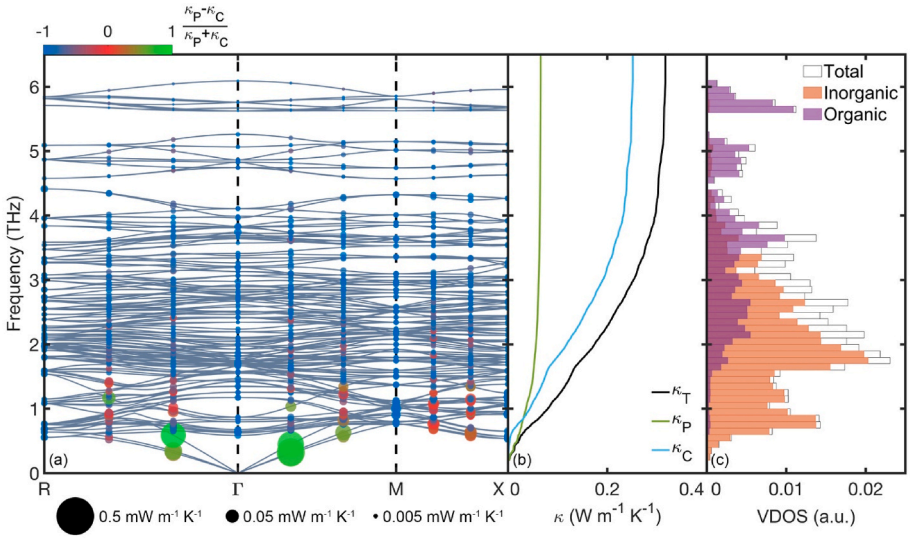

Fig. 3. (a) Phonon dispersion of the *I4/m* c-$MAPbI_3$ (grey lines) at 350 K. The colored circles represent the sampled phonon modes in the BZ. The area of each circle indicates the thermal conductivity contribution from a specified phonon mode. Its color identifies the contribution percentage to each channel [i.e., the light green means 100% population-channel (κ_P), the light blue means 100% coherence-channel (κ_C), and the red means equally to both channels]. Each κ_C value is distributed to the pair of phonons according to their heat capacity values. (b) The frequency-dependent cumulative thermal conductivity curves. (c) The vibrational density of states (VDOS) decomposed according to the inorganic and organic entities. Note that the phonon properties with frequencies above 6.5 THz are not shown for clarity.

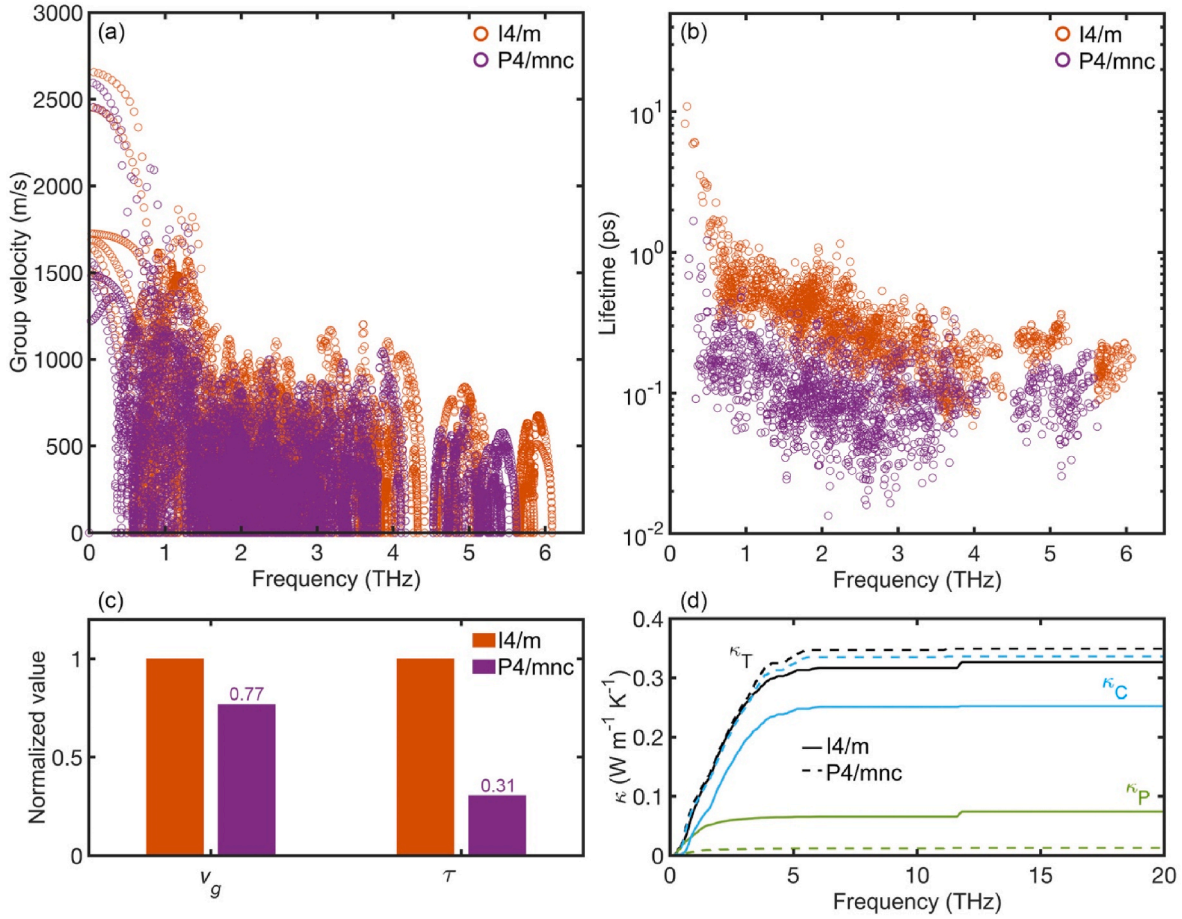

Fig. 4. Comparison of the (a) group velocity (v_g) and (b) lifetime (τ) between the *I4/m* and *P4/mnc* structures. Note that group velocities and lifetimes of phonons with frequencies above 6.5 THz are not shown for clarity. (c) The average v_g and τ from all the phonon modes are normalized with the corresponding average values from the *I4/m* structure. (d) The cumulative spectral κ_P, κ_C, and κ_T of the two optimized structures. The thermal conductivity contributions from phonons with a frequency higher than 20 THz are negligible.

P4/mnc structure did not produce a smaller κ_T, contradicting the intuitions from the PGM. We will probably need new indicators to intuitively capture the thermal conductivity of complex crystals in which the coherence-channel of phonons is dominant.

3. Conclusion

In summary, three optimized structures of c-$MAPbI_3$ that can produce real harmonic phonon dispersions are discovered. These structures are perhaps the first few for c-$MAPbI_3$ but are not the only ones possible. The maximum difference in the potential energy of these structures is below the thermal fluctuation energy at 350 K, making it possible for c-$MAPbI_3$ to vibrate and change into any of them. As a first check, these structures are verified by comparing their PDFs with existing experimental measurements. The calculated thermal conductivity values and temperature-invariant trend from MD and PWTE methods at temperatures above 327 K agree well with experimental measurements. Our analysis shows that the dominant contribution to the thermal transport in c-$MAPbI_3$ comes from the amorphous-like coherence-channel. This result explains why previous PBTE-based calculations that considered only the population-channel of phonons failed to reproduce the experimental results. The Debye temperature is found inadequate for determining the suitability of classical statistics in a thermal conductivity calculation for materials with a sizeable number of high-frequency optical modes that give significant coherence-channel contribution. We also show that the existing intuitions developed from the traditional PGM even fail to capture the thermal transport in complex hybrid crystals qualitatively. Two of our optimized structures have similar overall thermal conductivity values but vastly different population and coherence contributions. This result suggests a possible inter-channel conversion between population- and coherence-channel of phonons as c-$MAPbI_3$ vibrates through space at the same temperature. For this inter-channel conversion to be efficient/significant, the coherence-channel should have a considerable thermal conductivity contribution. This contribution typically arises from effective wave-tunneling between modes and strong phonons scattering. This inter-channel conversion will also offer a new direction to regulate thermal transport in $MAPbI_3$ and other structurally complex materials such as clathrates, skutterudites, and other perovskites. External fields or mechanisms that are known to affect the population-channel of the phonons may influence the coherence-channel of the phonons differently. Hence, different methods to modulate the coherence-channel contribution will be necessary to affect the overall thermal conductivity of hybrid complex crystals. Focusing on changing the phonon particles' group velocities and lifetimes may be insufficient. Such considerations will be critical for enhancing the performances of the hybrid crystals-based solar cells and thermoelectrics. Also, the present picture of the electron-phonon or plasmon-phonon interactions in hybrid perovskites may change with this non-traditional coherence-channel dominating the thermal transport process.

4. Computational methods

4.1. Non-equilibrium molecular dynamics

All MD simulations were performed in LAMMPS [54] using the MYP empirical potential [55]. This potential was verified to reproduce the experimental lattice constants [55] and thermal conductivity values of $MAPbI_3$ [9,10,21,56]. A time step of 0.5 fs was used. A three-dimensional periodic system was first simulated under an NPT ensemble for at least 1 ns to reach a zero bar pressure and the target temperature. This system was then equilibrated in an NVT ensemble and relaxed in an NVE ensemble for another 1 ns respectively. After relaxation, the Langevin thermostat, with a damping constant of 0.5 ps, was used in a NEMD simulation to calculate the thermal conductivity of the system. The temperature difference between the hot and cold reservoirs was 10%–15% of the system temperature. Each thermal reservoir was four conventional cubic unit cells long to match the selected thermostat damping constant [57,58]. The NEMD was performed for 10–20 ns to reach the steady-state condition for the different system sizes. The thermal conductivity was then calculated with the Fourier law using the data from the last 5 ns? A cross-sectional area of 6 × 6 and a length of 400 conventional cubic unit cells were needed to eliminate the finite-size effects (see Fig. S2). The standard deviation of each data point was calculated using from five independent runs with different initial seeds.

4.2. Structure optimization and characterization

By considering different combinations of the orientations of organic cations, about 50 different initial 2 × 2 × 2 cubic unit cell (lattice constants of $x = y = z = 12.59$ Å and angles of $\alpha = \beta = \gamma = 90°$) were created for optimization. Starting with many different initial structures increases the chance of getting more local minima structures. The lattice constants in these larger unit cells were averaged from an NPT ensemble at 350 K and 0 GPa to account for thermal expansion and not changed during the structure optimization. It is expected that the PES of such a 2 × 2 × 2 unit cell as compared to a 1 × 1 × 1 unit cell has a much larger degree of freedom and will be more complex. Thus, there will be more configurations with a local minimum potential energy. Our method involves two simple steps of applying existing LAMMPS commands. First, the conjugate gradient algorithm in LAMMPS was used to perform an energy minimization on these structures. It was previously found that a very flat PES around a local minimum prevents any structural relaxation algorithm finding the ground state configuration [36]. We then applied an energy dissipation procedure using the "fix viscous" command in LAMMPS to drain out the remaining kinetic energy caused by the residual forces [54]. The result of this step mirrors the goals of the frozen-phonon technique [36] but is simpler to implement. The pair distribution function was calculated using the method described in Ref. [13].

4.3. Interatomic force constants (IFCs) extraction

The ab initio-derived MYP potential [55] was used for the IFCs extraction in LAMMPS. The second-order IFCs were calculated using the finite-difference method [24] with a displacement of 0.001 Å. The third-order IFCs were calculated *via* the Taylor-series fitting method [24] by first removing the contributions of the second-order IFCs from the forces. The displaced structures were obtained using the thermal stochastic snapshot technique [59] at temperatures 1 K and 350 K for comparison. The resulting over-specified force-displacement linear system was solved using the least-square fit. We find that the difference in the predicted κ_T is within 6% for the different temperatures used in the thermal stochastic snapshot technique. The second-order force constant cutoff was chosen as 10.00 Å, similar to the force cutoff in this potential. The third-order force constant cutoff was chosen as 5.04 Å according to the convergence test results shown in Fig. S5a. Results from the convergence of the k-mesh with the BZ centered at the Γ point are plotted in Fig. S5b. A 6 × 6 × 6 k-mesh was selected. Only three-phonon scattering [22,23] under the single-mode relaxation time approximation [60] with no IFCs renormalization [59] was performed. A prior PWTE work [28] found such a calculation is sufficiently accurate to describe the thermal transport in a similar inorganic perovskite (i.e., $CsPbBr_3$). Representing the third-order IFCs in the k-space as $\Phi_{\lambda,\lambda',\lambda''}$, the three-phonon scattering rate for a specific phonon mode $\Gamma(\mathbf{q})_s$ can be expressed under the SMA using the Fermi's golden rule as:

$$\Gamma(\mathbf{q})_s = \frac{36\pi}{\hbar^2}\sum_{\lambda',\lambda''}\left|\Phi_{\lambda,\lambda',\lambda''}\right|^2 \times \left\{\begin{array}{c}(n_{\lambda'}+n_{\lambda''}+1)\delta(\omega_\lambda-\omega_{\lambda'}-\omega_{\lambda''}) \\ +(n_{\lambda'}-n_{\lambda''})[\delta(\omega_\lambda+\omega_{\lambda'}-\omega_{\lambda''})-\delta(\omega_\lambda-\omega_{\lambda'}+\omega_{\lambda''})]\end{array}\right\} \tag{1}$$

where $\hbar$ is the reduced Planck constant, each λ and its primes indicate a different phonon mode $(\mathbf{q},s)$, n is the Bose-Einstein distribution, and ω is the phonon frequency. δ is a function for enforcing energy conservation during a phonon scattering process.

In the PWTE [28], phonons contribute to the total thermal conductivity through two channels. The thermal conductivity from the population-channel comes from the particle-like propagation of phonons, as in the phonon Boltzmann transport equation. Under the single-mode relaxation time approximation, this thermal conductivity component can be written as:

$$\kappa^{\alpha,\beta}_{\mathrm{P,SMA}} = \frac{1}{V}\frac{\hbar^2}{k_B T^2}\sum_{\mathbf{q},s}\omega^2(\mathbf{q})_s n(\mathbf{q})_s\left(n(\mathbf{q})_s+1\right)v^\alpha(\mathbf{q})_{s,s}v^\beta(\mathbf{q})_{s,s}\Gamma(\mathbf{q})_s \tag{2}$$

where V is the volume of the system, k_B is the Boltzmann constant, T is temperature, α and β are Cartesian directions, $v^\alpha(\mathbf{q})_{s,s}$ is the group velocity of the phonon mode s with the wavevector $\mathbf{q}$ in the α direction.

The other thermal conductivity component is from the coherence-channel that arises from the wave-like behaviors of the phonons. This component is shown to be equivalent to the contributions from the diffusions in a harmonic glass of infinite volume. The thermal conductivity of this coherence-channel can be expressed as [28].

$$\kappa^{\alpha,\beta}_{\mathrm{C}} = \frac{1}{V}\frac{\hbar^2}{k_B T}\sum_{\boldsymbol{q}}\sum_{s,s'}\frac{\omega(\mathbf{q})_s+\omega(\mathbf{q})_{s'}}{2}v^\alpha(\mathbf{q})_{s,s'}v^\beta(\mathbf{q})_{s',s}\times\frac{\omega(\mathbf{q})_s n(\mathbf{q})_s\left(n(\mathbf{q})_s+1\right)+\omega(\mathbf{q})_{s'}n(\mathbf{q})_{s'}\left(n(\mathbf{q})_{s'}+1\right)}{4\left(\omega(\mathbf{q})_s-\omega(\mathbf{q})_{s'}\right)^2+\left(\Gamma(\mathbf{q})_s+\Gamma(\mathbf{q})_{s'}\right)^2}\times\left(\Gamma(\mathbf{q})_s+\Gamma(\mathbf{q})_{s'}\right) \tag{3}$$

where $v^{\alpha}(\mathbf{q})_{s,s'}$ is the coupling group velocity between the phonon modes s and s' of the same wavevector $\mathbf{q}$ in the α direction.

Credit author statement

Jin Yang: Investigation, Software, Visualization, Data Curation, Writing - Original Draft. **Ankit Jain:** Software, Validation, Writing-Reviewing and Editing. **Wee-Liat Ong:** Conceptualization, Supervision, Writing-Reviewing and Editing, Resources, Funding acquisition.

Declaration of competing interest

The authors declare that they have no known competing financial interests or personal relationships that could have appeared to influence the work reported in this paper.

Data availability

The optimized structures used for the calculations are uploaded as supporting files

Acknowledgements

W.-L. Ong was the principal supervisor supported by the National Natural Science Foundation of China [grant number 51876186 and 52150410417], Natural Science Foundation of Zhejiang Province [grant number LZ19E060002], ZJU-UIUC Institute, and the Zhejiang-Saudi EMC2 International Collaboration Laboratory.

Appendix A. Supplementary data

Supplementary data to this article can be found online at https://doi.org/10.1016/j.mtphys.2022.100892.

References

[1] T.M. Brenner, D.A. Egger, L. Kronik, G. Hodes, D. Cahen, Hybrid organic—inorganic perovskites: low-cost semiconductors with intriguing charge-transport properties, Nat. Rev. Mater. 1 (2016): 15007, https://doi.org/10.1038/natrevmats.2015.7.

[2] R. Lin, J. Xu, M. Wei, Y. Wang, Z. Qin, Z. Liu, J. Wu, K. Xiao, B. Chen, S.M. Park, G. Chen, H.R. Atapattu, K.R. Graham, J. Xu, J. Zhu, L. Li, C. Zhang, E.H. Sargent, H. Tan, All-perovskite tandem solar cells with improved grain surface passivation, Nature 603 (2022) 73–78, https://doi.org/10.1038/s41586-021-04372-8.

[3] X. Li, W. Zhang, X. Guo, C. Lu, J. Wei, J. Fang, Constructing heterojunctions by surface sulfidation for efficient inverted perovskite solar cells, Science 375 (2022) 434–437, https://doi.org/10.1126/science.abl5676.

[4] M. Younas, T.A. Kandiel, A. Rinaldi, Q. Peng, A.A. Al-Saadi, Ambient-environment processed perovskite solar cells: a review, Mater. Today Phys. 21 (2021): 100557, https://doi.org/10.1016/j.mtphys.2021.100557.

[5] S. Wang, F. Cao, W. Sun, C. Wang, Z. Yan, N. Wang, Z. Lan, J. Wu, A green Bi-Solvent system for processing high-quality CsPbBr3 films in efficient all-inorganic perovskite solar cells, Mater. Today Phys. 22 (2022): 100614, https://doi.org/10.1016/j.mtphys.2022.100614.

[6] M.A. Haque, S. Kee, D.R. Villalva, W. Ong, D. Baran, Halide perovskites: thermal transport and prospects for thermoelectricity, Adv. Sci. 7 (2020): 1903389, https://doi.org/10.1002/advs.201903389.

[7] C.C. Stoumpos, C.D. Malliakas, M.G. Kanatzidis, Semiconducting tin and lead iodide perovskites with organic cations: phase transitions, high mobilities, and near-infrared photoluminescent properties, Inorg. Chem. 52 (2013), https://doi.org/10.1021/ic401215x, 9019–9038.

[8] M. Massetti, F. Jiao, A.J. Ferguson, D. Zhao, K. Wijeratne, A. Würger, J. L. Blackburn, X. Crispin, S. Fabiano, Unconventional thermoelectric materials for energy harvesting and sensing applications, Chem. Rev. 121 (2021) 12465–12547, https://doi.org/10.1021/acs.chemrev.1c00218.

[9] T. Zhu, E. Ertekin, Mixed phononic and non-phononic transport in hybrid lead halide perovskites: glass-crystal duality, dynamical disorder, and anharmonicity, Energy Environ. Sci. 12 (2019) 216–229, https://doi.org/10.1039/C8EE02820F.

[10] M. Wang, S. Lin, Anisotropic and ultralow phonon thermal transport in organic–inorganic hybrid perovskites: atomistic insights into solar cell thermal management and thermoelectric energy conversion efficiency, Adv. Funct. Mater. (2016) 10.

[11] L.D. Whalley, J.M. Skelton, J.M. Frost, A. Walsh, Phonon anharmonicity, lifetimes, and thermal transport in CH 3 NH 3 PbI 3 from many-body perturbation theory, Phys. Rev. B 94 (2016): 220301, https://doi.org/10.1103/PhysRevB.94.220301.

[12] R. Comin, M.K. Crawford, A.H. Said, N. Herron, W.E. Guise, X. Wang, P. S. Whitfield, A. Jain, X. Gong, A.J.H. McGaughey, E.H. Sargent, Lattice dynamics and the nature of structural transitions in organolead halide perovskites, Phys. Rev. B 94 (2016): 094301, https://doi.org/10.1103/PhysRevB.94.094301.

[13] A.N. Beecher, O.E. Semonin, J.M. Skelton, J.M. Frost, M.W. Terban, H. Zhai, A. Alatas, J.S. Owen, A. Walsh, S.J.L. Billinge, Direct observation of dynamic symmetry breaking above room temperature in methylammonium lead iodide perovskite, ACS Energy Lett. 1 (2016) 880–887, https://doi.org/10.1021/acsenergylett.6b00381.

[14] C. Ge, M. Hu, P. Wu, Q. Tan, Z. Chen, Y. Wang, J. Shi, J. Feng, Ultralow thermal conductivity and ultrahigh thermal expansion of single-crystal organic–inorganic hybrid perovskite CH $_3$ NH $_3$ PbX $_3$ (X = Cl, Br, I), J. Phys. Chem. C 122 (2018), https://doi.org/10.1021/acs.jpcc.8b05919, 15973–15978.

[15] M.E. Manley, K. Hong, P. Yin, S. Chi, Y. Cai, C. Hua, L.L. Daemen, R.P. Hermann, H. Wang, A.F. May, M. Asta, M. Ahmadi, Giant isotope effect on phonon dispersion and thermal conductivity in methylammonium lead iodide, Sci. Adv. 6 (2020), https://doi.org/10.1126/sciadv.aaz1842 eaaz1842.

[16] A. Pisoni, J. Jaćimović, O.S. Barišić, M. Spina, R. Gaál, L. Forró, E. Horváth, Ultra-low thermal conductivity in organic–inorganic hybrid perovskite CH $_3$ NH $_3$ PbI $_3$, J. Phys. Chem. Lett. 5 (2014) 2488–2492, https://doi.org/10.1021/jz5012109.

[17] G.A. Elbaz, W.-L. Ong, E.A. Doud, P. Kim, D.W. Paley, X. Roy, J.A. Malen, Phonon speed, not scattering, differentiates thermal transport in lead halide perovskites, Nano Lett. 17 (2017) 5734–5739, https://doi.org/10.1021/acs.nanolett.7b02696.

[18] R. Heiderhoff, T. Haeger, N. Pourdavoud, T. Hu, M. Al-Khafaji, A. Mayer, Y. Chen, H.-C. Scheer, T. Riedl, Thermal conductivity of methylammonium lead halide perovskite single crystals and thin films: a comparative study, J. Phys. Chem. C 121 (2017) 28306–28311, https://doi.org/10.1021/acs.jpcc.7b11495.

[19] S.-Y. Yue, X. Zhang, G. Qin, J. Yang, M. Hu, Insight into the collective vibrational modes driving ultralow thermal conductivity of perovskite solar cells, Phys. Rev. B 94 (2016): 115427, https://doi.org/10.1103/PhysRevB.94.115427.

[20] X. Qian, X. Gu, R. Yang, Lattice thermal conductivity of organic-inorganic hybrid perovskite CH $_3$ NH $_3$ PbI $_3$, Appl, Phys. Lett. 108 (2016): 063902, https://doi.org/10.1063/1.4941921.

[21] Y. Gao, W. Ning, X. Zhang, Y. Liu, Y. Zhou, D. Tang, The effective regulation of nanotwinning on the multichannel thermal transport in hybrid organic–inorganic halide perovskite, Nano Energy 82 (2021): 105747, https://doi.org/10.1016/j.nanoen.2021.105747.

[22] A.A. Maradudin, A.E. Fein, Scattering of neutrons by an anharmonic crystal, Phys. Rev. 128 (1962) 2589–2608, https://doi.org/10.1103/PhysRev.128.2589.

[23] J.E. Turney, E.S. Landry, A.J.H. McGaughey, C.H. Amon, Predicting phonon properties and thermal conductivity from anharmonic lattice dynamics calculations and molecular dynamics simulations, Phys. Rev. B 79 (2009): 064301, https://doi.org/10.1103/PhysRevB.79.064301.

[24] A.J.H. McGaughey, A. Jain, H.-Y. Kim, Phonon properties and thermal conductivity from first principles, lattice dynamics, and the Boltzmann transport equation, J. Appl. Phys. 125 (2019): 011101, https://doi.org/10.1063/1.5064602.

[25] Y. Luo, X. Yang, T. Feng, J. Wang, X. Ruan, Vibrational hierarchy leads to dual-phonon transport in low thermal conductivity crystals, Nat. Commun. 11 (2020) 2554, https://doi.org/10.1038/s41467-020-16371-w.

[26] S. Mukhopadhyay, D.S. Parker, B.C. Sales, A.A. Puretzky, M.A. McGuire, L. Lindsay, Two-channel model for ultralow thermal conductivity of crystalline Tl $_3$ VSe $_4$, Science 360 (2018) 1455–1458, https://doi.org/10.1126/science.aar8072.

[27] W.-L. Ong, E.S. O'Brien, P.S.M. Dougherty, D.W. Paley, C. Fred Higgs III, A.J. H. McGaughey, J.A. Malen, X. Roy, Orientational order controls crystalline and amorphous thermal transport in superatomic crystals, Nat. Mater. 16 (2017) 83–88, https://doi.org/10.1038/nmat4739.

[28] M. Simoncelli, N. Marzari, F. Mauri, Unified theory of thermal transport in crystals and glasses, Nat. Phys. 15 (2019) 809–813, https://doi.org/10.1038/s41567-019-0520-x.

[29] M.N. Luckyanova, J. Garg, K. Esfarjani, A. Jandl, M.T. Bulsara, A.J. Schmidt, A. J. Minnich, S. Chen, M.S. Dresselhaus, Z. Ren, E.A. Fitzgerald, G. Chen, Coherent phonon heat conduction in superlattices, Science 338 (2012) 936–939, https://doi.org/10.1126/science.1225549.

[30] L. Yang, N. Yang, B. Li, Thermoelectric properties of nanoscale three dimensional Si phononic crystals, Int. J. Heat Mass Tran. 99 (2016) 102–106, https://doi.org/10.1016/j.ijheatmasstransfer.2016.03.096.

[31] D. Ma, A. Arora, S. Deng, G. Xie, J. Shiomi, N. Yang, Quantifying phonon particle and wave transport in silicon nanophononic metamaterial with cross junction, Mater. Today Phys. 8 (2019) 56–61, https://doi.org/10.1016/j.mtphys.2019.01.002.

[32] A. Jain, Multichannel thermal transport in crystalline Tl 3 VSe 4, Phys. Rev. B 102 (2020): 201201, https://doi.org/10.1103/PhysRevB.102.201201.

[33] Z. Zeng, C. Zhang, Y. Xia, Z. Fan, C. Wolverton, Y. Chen, Nonperturbative phonon scatterings and the two-channel thermal transport in Tl 3 VSe 4, Phys. Rev. B 103 (2021): 224307, https://doi.org/10.1103/PhysRevB.103.224307.

[34] Y. Xia, K. Pal, J. He, V. Ozoliņš, C. Wolverton, Particle like phonon propagation dominates ultralow lattice thermal conductivity in crystalline Tl 3 VSe 4, Phys. Rev. Lett. 124 (2020): 065901, https://doi.org/10.1103/PhysRevLett.124.065901.

[35] A.K. Bain, P. Chand, Ferroelectrics: Principles and Applications, Wiley-VCH Verlag GmbH & Co KGaA, Berlin, 2017.

[36] A. Marronnier, H. Lee, B. Geffroy, J. Even, Y. Bonnassieux, G. Roma, Structural instabilities related to highly anharmonic phonons in halide perovskites, J. Phys. Chem. Lett. 8 (2017) 2659–2665, https://doi.org/10.1021/acs.jpclett.7b00807.

[37] A. Marronnier, G. Roma, S. Boyer-Richard, L. Pedesseau, J.-M. Jancu, Y. Bonnassieux, C. Katan, C.C. Stoumpos, M.G. Kanatzidis, J. Even, Anharmonicity and disorder in the black phases of cesium lead iodide used for stable inorganic

perovskite solar cells, ACS Nano 12 (2018) 3477–3486, https://doi.org/10.1021/acsnano.8b00267.
[38] P. Souvatzis, O. Eriksson, M.I. Katsnelson, S.P. Rudin, Entropy driven stabilization of energetically unstable crystal structures explained from first principles theory, Phys. Rev. Lett. 100 (2008): 095901, https://doi.org/10.1103/PhysRevLett.100.095901.
[39] R.G. Della Valle, E. Venuti, Quasiharmonic lattice-dynamics and molecular-dynamics calculations for the Lennard-Jones solids, Phys. Rev. B 58 (1998) 206–212, https://doi.org/10.1103/PhysRevB.58.206.
[40] S.J.L. Billinge, M.G. Kanatzidis, Beyond crystallography: the study of disorder, nanocrystallinity and crystallographically challenged materials with pair distribution functions, Chem. Commun. (2004) 749–760, https://doi.org/10.1039/B309577K.
[41] K. Momma, F. Izumi, *VESTA 3* for three-dimensional visualization of crystal, volumetric and morphology data, J. Appl. Crystallogr. 44 (2011) 1272–1276, https://doi.org/10.1107/S0021889811038970.
[42] T. Feng, X. Ruan, Quantum mechanical prediction of four-phonon scattering rates and reduced thermal conductivity of solids, Phys. Rev. B 93 (2016): 045202, https://doi.org/10.1103/PhysRevB.93.045202.
[43] R. Hanus, J. George, M. Wood, A. Bonkowski, Y. Cheng, D.L. Abernathy, M. E. Manley, G. Hautier, G.J. Snyder, R.P. Hermann, Uncovering design principles for amorphous-like heat conduction using two-channel lattice dynamics, Mater. Today Phys. 18 (2021): 100344, https://doi.org/10.1016/j.mtphys.2021.100344.
[44] Z. Zhang, Y. Guo, M. Bescond, J. Chen, M. Nomura, S. Volz, Heat conduction theory including phonon coherence, Phys. Rev. Lett. 128 (2022): 015901, https://doi.org/10.1103/PhysRevLett.128.015901.
[45] M.T. Dove, Introduction to Lattice Dynamics, Cambridge University Press, New York, 1993.
[46] A. Kovalsky, L. Wang, G.T. Marek, C. Burda, J.S. Dyck, Thermal conductivity of $CH_3NH_3PbI_3$ and $CsPbI_3$: measuring the effect of the methylammonium ion on phonon scattering, J. Phys. Chem. C 121 (2017) 3228–3233, https://doi.org/10.1021/acs.jpcc.6b12231.
[47] P.K. Schelling, S.R. Phillpot, P. Keblinski, Comparison of atomic-level simulation methods for computing thermal conductivity, Phys. Rev. B 65 (2002): 144306, https://doi.org/10.1103/PhysRevB.65.144306.
[48] D.P. Sellan, E.S. Landry, J.E. Turney, A.J.H. McGaughey, C.H. Amon, Size effects in molecular dynamics thermal conductivity predictions, Phys. Rev. B 81 (2010): 214305, https://doi.org/10.1103/PhysRevB.81.214305.
[49] M. Li, Y. Yue, Molecular dynamics study of thermal transport in amorphous silicon carbide thin film, RSC Adv. 4 (2014): 23010, https://doi.org/10.1039/c4ra02985b.
[50] K. Sääskilahti, J. Oksanen, J. Tulkki, A.J.H. McGaughey, S. Volz, Vibrational mean free paths and thermal conductivity of amorphous silicon from non-equilibrium molecular dynamics simulations, AIP Adv. 6 (2016): 121904, https://doi.org/10.1063/1.4968617.
[51] W.-L. Ong, S. Majumdar, J.A. Malen, A.J.H. McGaughey, Coupling of organic and inorganic vibrational states and their thermal transport in nanocrystal arrays, J. Phys. Chem. C 118 (2014) 7288–7295, https://doi.org/10.1021/jp4120157.
[52] B. Kang, K. Biswas, Preferential $CH_3NH_3^+$ alignment and octahedral tilting affect charge localization in cubic phase $CH_3NH_3PbI_3$, J. Phys. Chem. C 121 (2017) 8319–8326, https://doi.org/10.1021/acs.jpcc.7b01184.
[53] A. Amat, E. Mosconi, E. Ronca, C. Quarti, P. Umari, MdK. Nazeeruddin, M. Grätzel, F. De Angelis, Cation-induced band-gap tuning in organohalide perovskites: interplay of spin–orbit coupling and octahedra tilting, Nano Lett. 14 (2014) 3608–3616, https://doi.org/10.1021/nl5012992.
[54] A.P. Thompson, H.M. Aktulga, R. Berger, D.S. Bolintineanu, W.M. Brown, P. S. Crozier, , P.J. in 't Veld, A. Kohlmeyer, S.G. Moore, T.D. Nguyen, R. Shan, M. J. Stevens, J. Tranchida, C. Trott, S.J. Plimpton, Lammps - a flexible simulation tool for particle-based materials modeling at the atomic, meso, and continuum scales, Comput. Phys. Commun. 271 (2022): 108171, https://doi.org/10.1016/j.cpc.2021.108171.
[55] A. Mattoni, A. Filippetti, M.I. Saba, P. Delugas, Methylammonium rotational dynamics in lead halide perovskite by classical molecular dynamics: the role of temperature, J. Phys. Chem. C (2015) 8.
[56] C. Caddeo, C. Melis, M.I. Saba, A. Filippetti, L. Colombo, A. Mattoni, Tuning the thermal conductivity of methylammonium lead halide by the molecular substructure, Phys. Chem. Chem. Phys. 18 (2016) 24318–24324, https://doi.org/10.1039/C6CP04246E.
[57] Z. Li, S. Xiong, C. Sievers, Y. Hu, Z. Fan, N. Wei, H. Bao, S. Chen, D. Donadio, T. Ala-Nissila, Influence of thermostatting on nonequilibrium molecular dynamics simulations of heat conduction in solids, J. Chem. Phys. 151 (2019): 234105, https://doi.org/10.1063/1.5132543.
[58] W.-J. Chen, B. Feng, C. Shao, J. Yang, L. Fan, W.-L. Ong, I.-L. Chang, Asymmetrical carbon nanotubes exhibit opposing thermal rectification behaviors under different heat baths, Int. J. Heat Mass Tran. 184 (2022): 122341, https://doi.org/10.1016/j.ijheatmasstransfer.2021.122341.
[59] N.K. Ravichandran, D. Broido, Unified first-principles theory of thermal properties of insulators, Phys. Rev. B 98 (2018): 085205, https://doi.org/10.1103/PhysRevB.98.085205.
[60] A. Chernatynskiy, S.R. Phillpot, Evaluation of computational techniques for solving the Boltzmann transport equation for lattice thermal conductivity calculations, Phys. Rev. B 82 (2010): 134301, https://doi.org/10.1103/PhysRevB.82.134301.